Growth kinetics of crumb-like structure formation on SnO$_2$ nanowires during direct oxidation

Vivekanandan Alangadu Kothandan [a,b], Chang Shao-Fu [b], Li Zhong-You [b], Chen Shih-Hsun [b,*]

[a] Department of Aeronautical Engineering, Annasaheb Dange College of Engineering and Technology, Ashta, Sangli, 416301, Maharashtra, India
[b] Department of Mechanical Engineering, National Yang Ming Chiao Tung University, Hsinchu 300039, Taiwan

ARTICLE INFO

ABSTRACT

A facile AAO (anodic aluminum oxide) template-assisted vacuum die-casting technique was used to create Sn nanowires and convert them into SnO$_2$ without degrading the wires nanostructure. As a function of time and temperature, the controlled oxidation on the Sn nanowires of two different spatial configurations (100 and 250 nm in diameter) revealed distinct oxidation mechanisms. The 250-SnO$_2$ nanowires exhibits a peculiar crumb-like structure formation over the surface due to the higher level of Sn atom dislocation. Conversely, the sub-100 nm SnO$_2$ nanowires shows a highly crystalline, homogenous, and defect-free surfaces. The optical properties of the sub-100 nm SnO$_2$ nanowires were characterized using UV–Vis spectroscopy. The heat-treated tin oxides nanowires samples at temperatures of 300, 500, and 700 °C for 7 h exhibited optical energy bandgaps of 1.8, 2.6, and 3.3 eV, respectively. The observed variation in bandgap is attributed to the unique phase compositions achieved in each of the heat-treated samples. Moreover, the obtained results showed exceptional structural integrity and optical properties that are inherently interconnected with the diverse phases achieved under precise heat treatment conditions.

1. Introduction

In recent decades, nanowires have emerged as versatile materials with applications spanning optoelectronics, thermoelectrics, gas sensing, and energy storage devices [1–5]. Their unique properties, such as high aspect ratio, large surface-to-volume ratio, and quantum confinement effects, have made nanowires indispensable for diverse technological advancements [6,7]. The influence of nanowire size at the nanoscale level induces substantial changes in optical and electronic properties, leading to notable alterations in bandgap and electrical characteristics [8,9]. Consequently, precise control over material phase composition and phase transition processes during nanowire synthesis significantly influences their structural, electronic, and mechanical attributes. Achieving optimal process parameters in nanowire fabrication stands as a pivotal challenge for material engineers [10,11]. This holds particularly true for semiconductor metal oxide nanowires, wherein kinetic control of oxide formation plays a crucial role in modulating dimensional crystal growth and nucleation. Notably, the electronic and transport properties of these nanowires are heavily contingent on their shape and surface charge carriers. Thus, a thorough investigation into the geometry and controlled phase composition of metal oxide nanowires presents considerable potential for developing innovative materials tailored for future device applications.

---

* Corresponding author.
E-mail address: brucechen@nycu.edu.tw (C. Shih-Hsun).

Among semiconductor metal oxides, SnO_2 has garnered remarkable attention due to its exceptional attributes: a wide bandgap energy (3.6 eV), high oxidation potential, chemical inertness, non-toxicity, cost-effectiveness, and environmental compatibility [12–14]. Diverse techniques, including hydrothermal, sol-gel, and template-assisted electrodeposition methods, have been employed to fabricate SnO_2 nanowires [15–17]. Within these approach, the Anodic Aluminum Oxide (AAO) template-assisted die-casting method offers an accessible, cost-effective, and efficient approach for nanowires fabrication. In this process, molten metal is injected into an electrochemically fabricated AAO template under high pressure, thereby replicating the pore structure geometry [18–20].

The rapid cooling of molten metal within AAO nanochannels confines the metal to the interior, inducing outer oxide formation on the nanowires. The nanowires generated within the template are typically removed using a chemical etching method. Subsequently, a kinetically controlled oxidation process is employed to produce metal oxide nanowires. However, it is imperative to acknowledge that Sn exhibits high sensitivity to thermal oxidation, leading to the formation of various coaxial core-shell metastable phases and sub-oxides [21–23]. At temperatures exceeding 350 °C, nanowires undergo oxidation, yielding orthorhombic and tetragonal phases of SnO_2, unlike bulk Sn which forms stable tetragonal rutile SnO_2 under ambient pressure. The presence of the orthorhombic structure signifies the high internal pressure within the oxide shell during oxygen diffusion. Moreover, the dislocation of Sn atoms in the oxide core plays a pivotal role in determining the shape and integrity of SnO_2 nanowires [24,25].

Notably, the existence of different crystalline phases within SnO_2 nanowires holds a predominant influence over their optical properties, particularly their optical bandgaps. The distinct electronic structures and lattice arrangements associated with these phases contribute to variations in the energy required for electrons to transition from the valence band to the conduction band. Consequently, the optical bandgap of SnO_2 nanowires can vary depending on whether they are predominantly in the orthorhombic or tetragonal phase [26–28]. This phenomenon has implications for the nanowires performance in optoelectronic applications, as their responsiveness to different wavelengths of light is closely linked to their optical bandgap characteristics.

Herein, our work aims to address a critical gap in understanding the controlled structure-preserving thermal oxidation of SnO_2 nanowires produced through the AAO template-assisted vacuum die-casting method. Specifically, we delve into the influence of Sn nanowires crystalline phase formation and structural integrity on thermal oxidation processes. Through meticulous examination of nanowire oxidation at varying temperatures and durations, the formation of unique phases and morphologies has been investigated. The empirical relation between an optical bandgap and crystalline phase of SnO_2 nanowires were identified.

2. Experimental procedure

2.1. AAO-template fabrication

To fabricate the AAO template, a two-step anodization process was employed. Commercial grade aluminum foil (99.7% purity) with dimensions of 5×0.3 cm was used as the substrate. Prior to anodization, the aluminum (Al) substrate underwent pre-processing, including ultrasonic treatment and electropolishing, to achieve a highly polished, uniform, and defect-free surface. The first electrochemical anodization was performed in a 3 wt% oxalic acid solution at a constant voltage of 40 V for 1 h in anodization cell with Al foil as the anode and an Al sheet as the cathode. After the first anodization, the resulting substrate was immersed in a solution containing 1.8 wt% chromic acid and 6 vol% phosphoric acid for 1 h at a 60 °C. Subsequently, the second anodization was carried out under the same conditions as the first, applying a constant voltage for 48 h. Following the second anodization, pore widening was performed by immersing the substrate in a 5 wt% phosphoric acid solution for 1 h. To remove any remaining Al from the substrate, a 5 vol% HCl and 8 wt% $CuCl_2$ aqueous solution was used. A similar process was repeated for the production of the AAO template using a phosphoric acid electrolyte with a constant voltage of 150 V and a second anodization time of 96 h.

2.2. Synthesis of SnO_2 nanowires

Sn nanowires were generated within the nanochannels of the AAO template using a vacuum die-casting process. The AAO template was positioned in a vacuum chamber, and fragments of 99.99% pure Sn were uniformly distributed on top. The temperature of the chamber was gradually increased to 282 °C (melting point of Sn is 231.9 °C) and held for a specific duration. Subsequently, the system was cooled to room temperature (26 °C) while applying hydraulic pressure (50 kg/cm^2) to ensure the uniform infiltration of molten Sn into the nanopores of the AAO template. The resulting Sn/AAO template was immersed in an aqueous solution (1.8 wt% chromic acid + 6 vol% phosphoric acid) for 5 h at 60 °C for the AAO dissolution. After the dissolution, the solution underwent sonication and centrifugation for 20 min to collect the Sn nanowires. The obtained Sn nanowires were then subjected to a thermal conversion process in a furnace to form SnO_2 nanowires. The conversion process involved varying combinations of time and temperature to optimize the SnO_2 nanowires.

2.3. Fabrication of SnO_2 nanowire device

The synthesized SnO_2 nanowires were transferred onto a SiO_2 substrate patterned with Au electrodes for interconnections. Focused Ion Beam (FIB) was selectively used to deposit Pt metal, enabling the binding of the SnO_2 nanowires to an Au electrode using a trimethyl-zyl-cyclopentadienyl-platinum $(CH_3)_1$ Pt $(CpCH_3)$ injector. The as-prepared nanowire device was then used to measure the optical characteristics of SnO_2.

2.4. Characterization

The microstructural analysis of the AAO templates, Sn nanowires, and SnO$_2$ nanowires was conducted using field-emission scanning electron microscopy (FESEM, JSM-6900F) and high-resolution transmission electron microscopy (HRTEM, JEM-2010). The rate of phase transformation was determined using the BRUKER D2 PHASER-X-ray diffraction (XRD) instrument. Furthermore, the FEI Versa 3D HR-Dual Beam instrument was utilized for the fabrication of single SnO$_2$ nanowire devices.

3. Result and discussion

3.1. Morphological and microstructural analysis

Typical Sn nanowires grown in the AAO template replicate the nanochannel pore structure, where the diameter of the pore channel is adjusted by acid electrolytes [29]. The honeycomb nanostructures of the high aspect ratio AAO-template were fabricated in oxalic and phosphoric electrolytes; the averaged pore dimensions are about 100 nm and 250 nm, respectively, as shown in Fig. 1(a)-(c). The AAO-template was used as a nanomold in the vacuum die-casting method. High pressure and a temperature of 282 °C for 30 min were adopted for melting the bulk Sn to flow homogeneously into the high aspect ratio nanochannels. While the molten Sn flows deeper into the nanochannels, it subsequently cooled down to room temperature to generate nanowires. The Sn nanowires were extracted from AAO-templates by a chemical etching process as shown in Fig. 1(d) and 1(e and f) further show the magnification images of single nanowire with diameters of 250 nm (250-Sn) and 100 nm (100-Sn), respectively. The as-prepared nanowires possess a straight and orderly structure, and are enveloped by an oxide shell formed during the AAO dissolving process, as shown in Fig. 1 (g). This oxide shell enables the Sn nanowires to retain their shape at higher temperatures, facilitating liquid phase reactions.

To achieve high-quality tin oxide (SnO$_2$) nanowires, the as-synthesized Sn nanowires underwent heat treatment at different temperatures and durations in an air oven. The resulting phase transformation and crystallographic features were determined using XRD analysis, as depicted in Fig. 2. Fig. 2(a and b) illustrates the XRD patterns obtained from Sn nanowires with diameters of 100 nm and 250 nm, respectively. The nanowires were subjected to heat treatment in the temperature range of 200–700 °C for a duration of 7 h. The Sn nanowires that were grown in the AAO nanochannel exhibited a strong 200 peak, which was attributed to crystallization along the [100] direction (Fig. 2(a) and b). The reason for the high crystallinity is the nucleation growth of the Sn atom in the AAO pore structure caused by the confinement effect. Besides, the variation of the 200 and 101 diffraction signals denotes the concentration of the Sn atom confinement difference in the pore wall. Typically, nanowires with larger diameters (250-Sn) have a stronger diffraction peak at 200 (Fig. 2(b)) than thinner ones (100-Sn).

In Fig. 2 (a & b), the Sn metallic nanowires shown no change in phase constitution after experiencing solid-state heat treatment at 200 °C for 7 h. When Sn nanowires are oxidized above their melting point (231.9 °C), all three suboxides of Sn phases coexist. As the temperature rises to 400 °C, the intensity of the romarchite SnO peak disappears while the strength of the Sn$_3$O$_4$ peak increases, and the SnO$_2$ tetragonal structure begins to appear. Whereas the intensity of Sn is reduced, revealing the change in crystallinity and the growth of new phase nucleation in the nanowires. Thus, the relatively slow growth of the tin oxides (Sn$_3$O$_4$ and SnO$_2$) indicates that the oxidation is kinetically controlled. During the oxidation process, the oxide growth initiates from the surface grain boundaries of the nanowires and diffuses inward towards the metallic Sn, which completely transforms at 500 °C to form SnO$_2$ tetragonal phase. When oxidation was carried out at 700 °C, the strong SnO$_2$ tetragonal phase and orthorhombic phase co-exist. Particularly, the 250-SnO$_2$ nanowire elucidates a predominant sharp peak compared to the 100-SnO$_2$ oxidation at 700 °C. It can be concluded from the existence of the orthorhombic phase that the molten tin rapidly cooled in the template, forming an outer oxide layer and an inner metallic tin due to the high pressure generated in the core-shell during the oxidation [26].
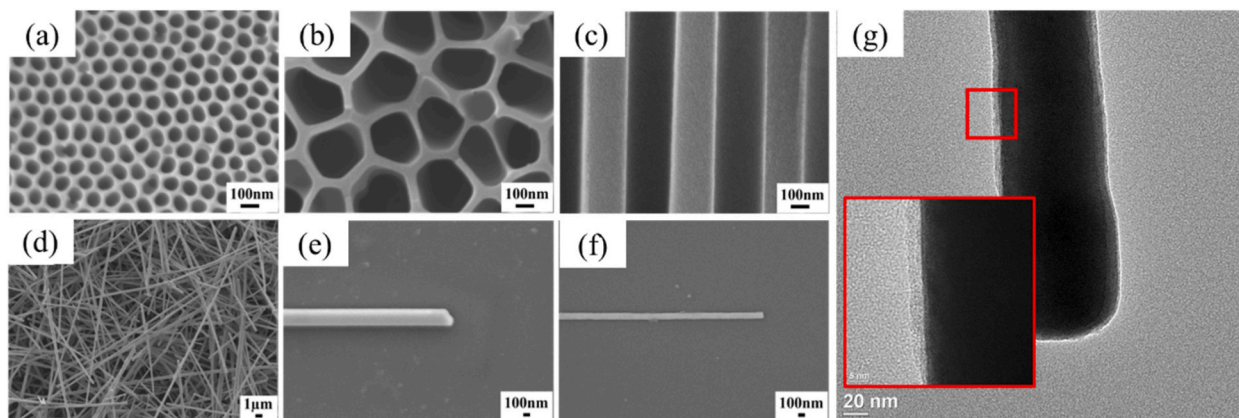
Fig. 1. Top-view SEM images of AAO templates fabricated in (a) oxalic acid and (b) phosphoric acid electrolytes, and (c) cross-sectional morphology of AAO template prepared in phosphoric acid, (d) the Sn nanowires extracted from AAO template, (e) single nanowire extracted from oxalic AAO template and (f) phosphoric AAO template (g) Enlarged TEM image of single Sn nanowire covered by oxide shell.
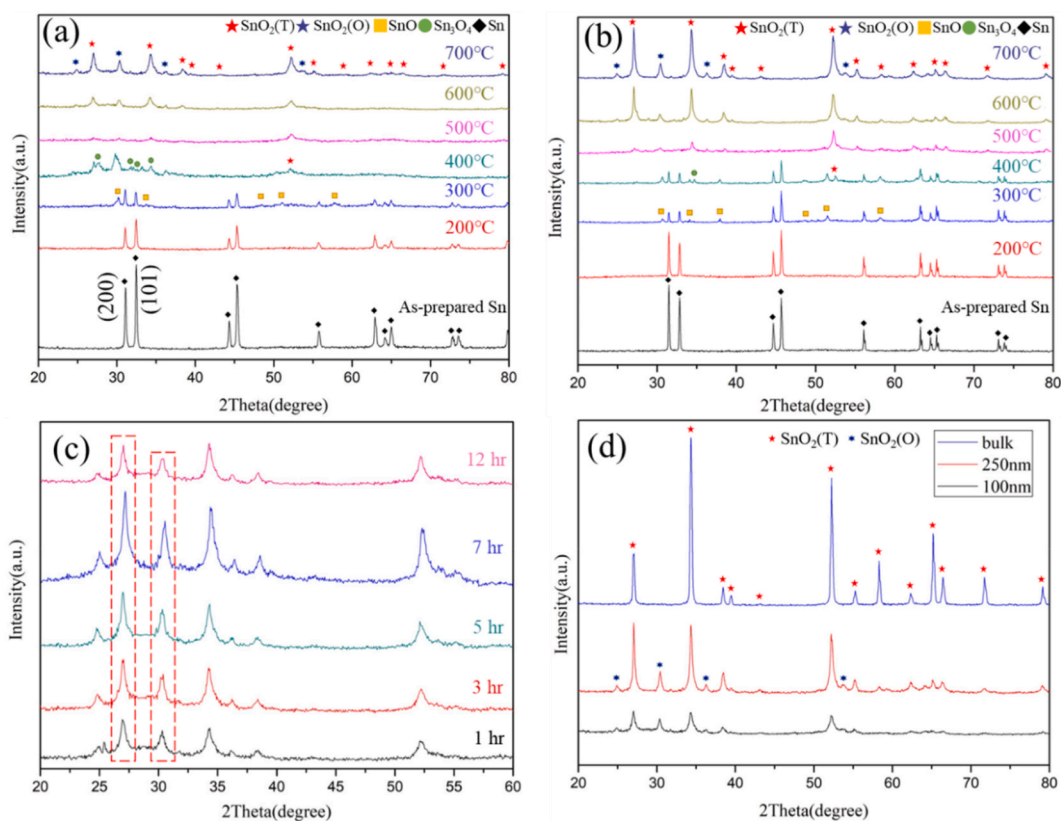
Fig. 2. XRD patterns obtained for (a) 100 nm and (b) 250 nm diameter SnO_2 nanowires oxidized at different temperatures for 7 h. The spectra (c) varied with oxidation times of 100-SnO_2 at 700 °C for 1–12 h, and (d) XRD pattern of SnO_2 bulk, 100-SnO_2, and 250-SnO_2 nanowires heat treated at 700 °C for 7 h.

In order to determine the crystallographic structure of 100-SnO_2 nanowires, the oxidation at 700 °C over various time intervals of 1–7 h was carried out. The oxidation time difference reveals a significant impact on the crystallinity of the SnO_2, as shown in Fig. 2(c). For 7h heat treated samples, the SnO_2 nanowire exhibits a predominant tetragonal peak, which illustrates the formation of a stable phase. Furthermore, Fig. 2(d) depicts the peculiar phase composition of bulk, 100, and 250-SnO_2 nanowires after 7 h of oxidation at 700 °C. The SnO_2 nanowires exhibit both orthorhombic and tetragonal phase structures, whereas the bulk SnO_2 shows a tetragonal phase. In SnO_2 nanowires, the weak orthorhombic phases are identified; however, the greater concentration of Sn atoms in 250-SnO_2 prevents their formation. A broad diffraction signal of 100-SnO_2 nanowires illustrates the lower crystallinity or higher defect density during the oxidation process. The core-shell oxide formation may occurs due to the rapid cooling of Sn nanowires, revealing the orthorhombic SnO_2 structure growth in the nanowires. To understand the formation mechanism, the topological influence of oxidation on Sn nanowires has been studied using TEM analysis.

Fig. 3 exhibits TEM images of separated nanowires and their SAED patterns after 7 h of oxidation at 700 °C**.** The sub-100 nm diameter nanowire in Fig. 3(a) and (b) has remarkably smooth and uniform preferential direction. The corresponding SAED pattern marked in Fig. 3(c) shows the lattice fringes of SnO_2 along the crystal planes (110), (200), and (220) in the direction [001]. The obtained results confirm the existence of tetragonal and orthorhombic phases of 100-SnO_2 nanowire. Whereas the 250-SnO_2 nanowire in Fig. 3(d) and (e) shows an irregular dent or oxide burst formation in the nanowire. The diffraction pattern, in Fig. 3 (f), indicates (110), (101), (200), and (211) planes associated with the tetragonal phase and the accumulation of inferior orthorhombic crystal structures, which is consistent with the XRD results. Based on TEM analysis, the circumference of the Sn nanowires has a significant impact on their shape and integrity of SnO_2 nanowires after oxidation at 700 °C. The low-diameter SnO_2 nanowires exhibit superior geometry and structural fidelity during oxidation which may result in enhanced electronic properties.

The Sn nanowires obtained through the AAO-assisted die casting process are surrounded by an oxide shell, the thickness of which is primarily determined by the wet-etching time. In the case of 250-SnO_2 nanowires, the larger volume induces higher expansion stress during oxidation, leading to localized perturbations within the confined region of the oxide shell (Fig. 3(c)). This is in contrast to the thinner nanowires (Fig. 3(d)). SEM images in Fig. 4(a) and (b) exhibit distinct appearances of 100 and 250-SnO_2 nanowires after being oxidized at 700 °C for 7 h. The excessive stresses cause liquid Sn to breach the 250-Sn oxide, resulting in oxide growth or referred to as oxide burst. However, sub-100 nm SnO_2 nanowires with a lower concentration of Sn atoms exhibit high homogeneity, precision, and shape integrity in the template-assisted vacuum die-casting fabrication process. Therefore, the 100-SnO_2 nanowires were further
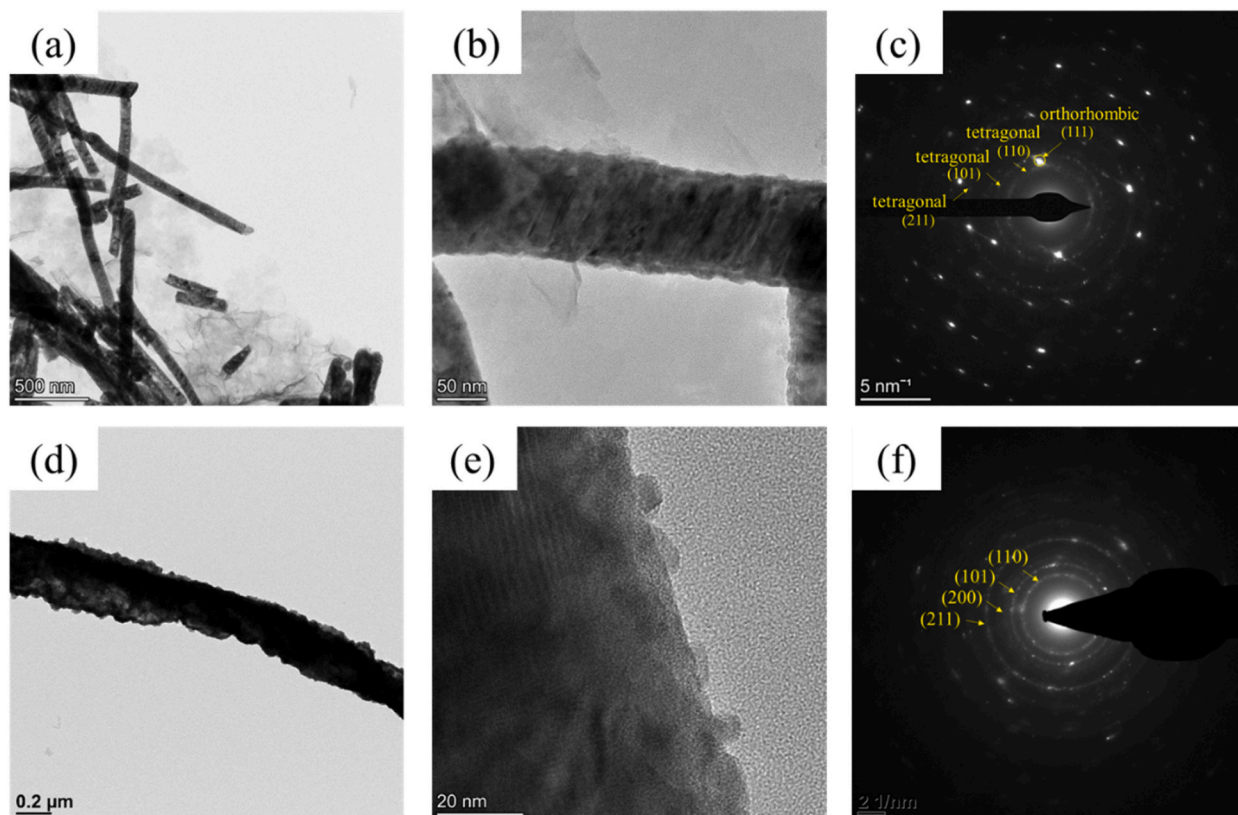
Fig. 3. (a) TEM image of 100-SnO$_2$ nanowires, (b) magnified image of a single nanowire from 100-SnO$_2$ nanowires, and (c) selected area diffraction pattern for 100-SnO$_2$ nanowires. (d) TEM image of 250-SnO$_2$ nanowires, (e) magnified image of a single nanowire from 250-SnO$_2$ nanowires, and (f) selected area diffraction pattern for 250-SnO$_2$ nanowires.
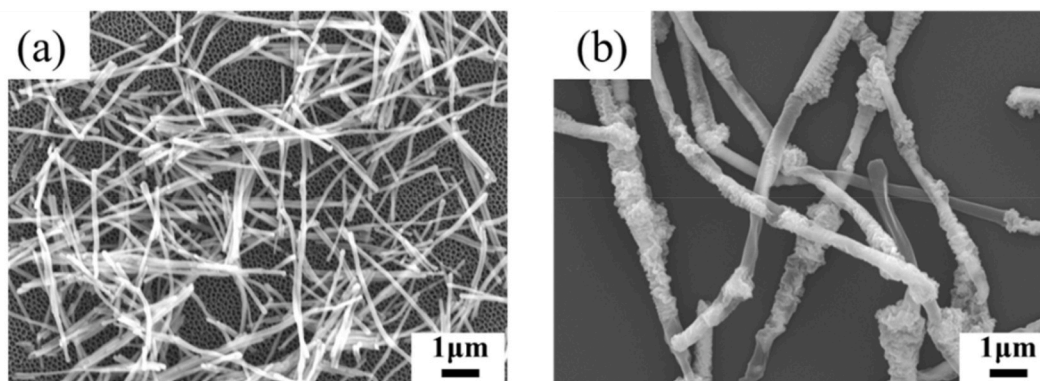

Fig. 4. SEM images of (a) 100-SnO$_2$ and (b) 250-SnO$_2$ nanowires.

employed to determine the optical energy bandgap.

3.2. Optical property of SnO$_2$ nanowires

The optical properties of 100 nm tin oxide nanowires were investigated using UV–vis spectroscopy. In Fig. 5(a), the absorbance variation with wavelength is shown for tin oxide nanowires oxidized at 300, 500, and 700 °C. This spectrum provides valuable information about the optical energy bandgap of the tin oxide nanowires. It is noteworthy that the absorption signal shifted towards higher energy levels with an increase in oxidation temperature. This shift can be attributed to surface voids, agglomeration of Sn atoms, and the phase transformation of the tin oxide nanowires due to different oxidation temperature.
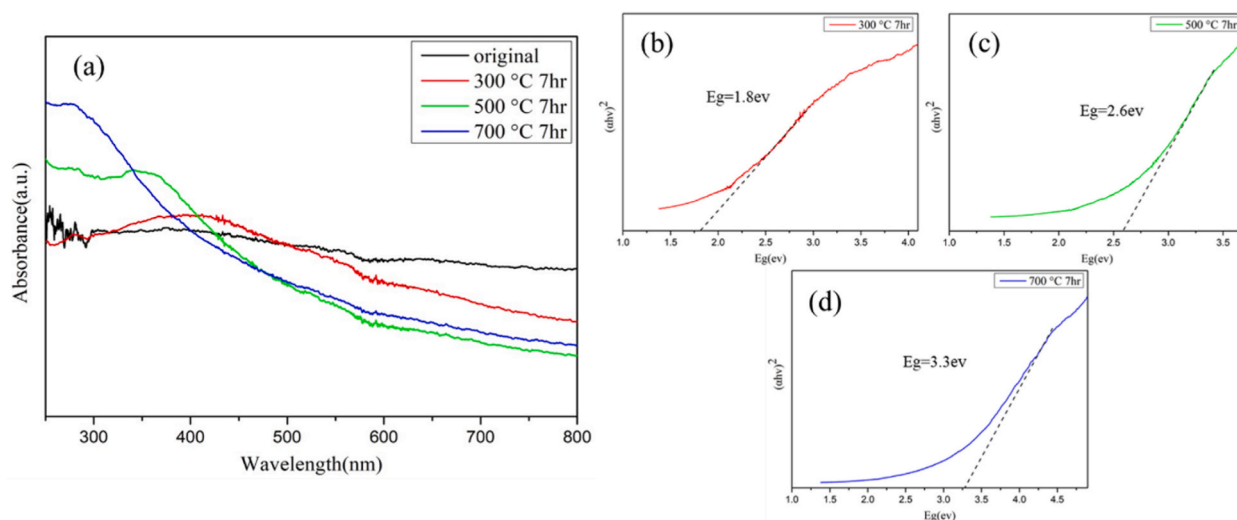
Fig. 5. Absorption spectra of SnO_2 nanowires under different oxidation treatment conditions (a) and (b–d) bandgap determination of 100-SnO_2 annealed at 300, 500, and 700 °C for 7 h.

Fig. 5(b)–(d) represent the optical energy bandgap of 100 nm tin oxide nanowires from the $(\alpha h\nu)2$–$(h\nu)$ plots. Tin oxide nanowires heat-treated at 300, 500, and 700 °C for 7h exhibited optical energy bandgaps of 1.8, 2.6, and 3.3 eV, respectively. These results clarify that increasing the oxidation temperature led to an increase in the tin oxide nanowire bandgap energy. The tin oxide nanowire forms distinct phases at different oxidation temperatures, which has been clearly illustrated in XRD analysis. At 300 °C, tin oxide nanowires exhibit Sn and SnO phases, leading to a reduction in the bandgap due to the metallic phase. At 500 °C, the stable sub-oxides of the metal disappear, initiating the growth of the tetragonal structure of SnO_2. Subsequently, at 700 °C, there is a predominant growth of the SnO_2 tetragonal phase and an accumulation of the orthogonal phase, resulting in an increased bandgap energy of 3.3 eV. The obtained result reveals that the phase composition of the tin oxide nanowires has a significant impact on the bandgap energy. Predominantly, the electronic states at the edges of the conduction and valence bands can be adjusted through oxidation, widening the forbidden band. This, in turn, enhances electron transfer by shifting more positions to a negative value of the conduction band [36]. The empirical analysis highlights the significance of tin oxide nanowires, as the resulting bandgap energy can be tailored through phase formation in the kinematically controlled oxidation process. Table 1 presents a comparative analysis of the optical bandgaps of SnO_2 nanoparticles fabricated through various techniques. In these different synthesis methods, such as AAO/Sol-gel, Electrospinning, and Template-assisted deposition, the tetragonal SnO_2 phase emerges as the predominant crystal structures [28–32]. It implies that the weak orthorhombic phase in SnO_2 nanowire is responsible for the 3.3 eV optical bandgap energy when compared to other works. Thus, the AAO template-assisted vacuum die-casting process enables the production of precise phase controllable tin oxide nanowires for applications in optoelectronics.

4. Conclusion

In summary, SnO_2 one-dimensional nanomaterials have been successfully fabricated using the AAO template-assisted vacuum die-casting technique and kinematically controlled oxidation. SEM analysis illustrates the shape integrity of SnO_2 nanowires of sub 100 nm and 250 nm diameters heat-treated at 700 °C. The SnO_2 protuberance or crumb-like structure growth on the surface for nanowires with higher diameter, while the sub 100 nm shows high crystalline homogeneous growth due to the low Sn atom dislocation during oxidation. TEM analysis confirms the amorphous, polycrystalline SnO_2 nanowires manufactured. The UV–Vis spectroscopy analysis determined the optical property of the SnO_2 nanowires, illustrating a absorption in the UV range. The heat treated tin oxide nanowire samples at 300, 500, and 700 °C for 7h exhibited optical energy bandgaps of 1.8, 2.6, and 3.3 eV, respectively. The observed variation in bandgap is attributed to the distinct phase compositions achieved in each of the heat-treated samples. Overall, the outcomes of this study highlight the potential of the vacuum die-casting template method to produce SnO_2 nanowires with adjustable optical properties through precise control of phase and structural integrity.

Author contribution statement

Alangadu Kothandan Vivekanandan: Conceived and designed the experiments; Wrote the paper.
Shao-Fu Chang; Zhong-You Li: Performed the experiments; Analyzed and interpreted the data.
Shih-Hsun Chen: Contributed reagents, materials, analysis tools or data; Wrote the paper.

Table 1

Comparison of optical band gap of SnO$_2$ nanowires fabricated from various template assisted techniques.

Nanoparticles	Synthesis method	Band gap (eV)	Reference
SnO$_2$ 1D Nanostructure	AAO/Sol-gel	3.6	[30]
SnO$_2$ 1D nanostructures	Electrospinning/sol–gel method	3.3–3.8	[31]
SnO$_2$ nanorods	AAO/immerse and filtration technique	3.9	[32]
SnO$_2$ nanowires	AAO/Liquid phase deposition	3.2–3.8	[33]
SnO2 nanofibers	Electrospinning	3.3	[34]
SnO$_2$ nanowires	Chemical template/Sol-gel	2.4	[35]
SnO2 nanowires	**AAO/Vacuum die-casting technique**	**1.8–3.3**	**Current work**

Data availability statement

Data will be made available on request.

Declaration of competing interest

The authors declare that they have no known competing financial interests or personal relationships that could have appeared to influence the work reported in this paper.

Acknowledgment

References

[1] J.Y. Chen, M.C. Wu, Y.H. Ting, W.C. Lee, P.H. Yeh, W.W. Wu, Applications of p-n homojunction ZnO nanowires to one-diode one-memristor RRAM arrays, Scr Mater 187 (2020) 439–444, https://doi.org/10.1016/J.SCRIPTAMAT.2020.06.061.

[2] S. Zhang, L. Ci, W. Mu, Hydrothermal synthesis of Ag2Cu(VO3)4/Ag nanowires: a new cathode material for lithium-ion batteries, Scr Mater 210 (2022), 114431, https://doi.org/10.1016/J.SCRIPTAMAT.2021.114431.

[3] S.H. Chen, C.Y. Wang, Y.C. Chen, C.W. Hun, S.F. Chen, S.M. Yang, Fabrication of pure aluminum nanowires by using injection molding process in ambient air, Mater. Lett. 148 (2015) 30–33, https://doi.org/10.1016/j.matlet.2015.02.082.

[4] A.K. Vivekanandan, B.-R. Huang, D. Kathiravan, A. Saravanan, A. Prasannan, H.-C. Tsai, S.-H. Chen, Effect of MoS2 solution on reducing the wall thickness of ZnO nanotubes to enhance their hydrogen gas sensing properties, J. Alloys Compd. 854 (2021), https://doi.org/10.1016/j.jallcom.2020.157102.

[5] J.W. Roh, J. Ham, J. Kim, H. Moon, H.S. Kim, W. Lee, Extreme reduction of thermal conductivity by embedding Al2O3 nanoparticles into single-crystalline Bi nanowires, Acta Mater. 136 (2017) 315–322, https://doi.org/10.1016/J.ACTAMAT.2017.07.020.

[6] D. Cavalcoli, M.A. Fazio, Electronic transitions in low dimensional semiconductor structures measured by surface photovoltage spectroscopy, Mater. Sci. Semicond. Process. 92 (2019) 28–38, https://doi.org/10.1016/J.MSSP.2018.05.027.

[7] L. Gu, P. Caroff, A. Fontcuberta I Morral, Vapor Phase Growth of Semiconductor Nanowires: Key Developments and Open Questions, 2019, https://doi.org/10.1021/acs.chemrev.8b00649.

[8] C. Jia, Z. Lin, Y. Huang, X. Duan, Nanowire electronics: from nanoscale to macroscale, Chem Rev 119 (2019) 9074–9135, https://doi.org/10.1021/ACS.CHEMREV.9B00164/ASSET/IMAGES/ACS.CHEMREV.9B00164.SOCIAL.JPEG_V03.

[9] Y. Zhang, Y. Xue, K. Qi, Z. Ru, J. Cai, W. Chen, Construction of various one-dimensional ZnS/MnS heteronanostructures with varied diameters via the multistep solution-solid-solid growth method, Inorg. Chem. 61 (2022) 1152–1158, https://doi.org/10.1021/ACS.INORGCHEM.1C03431.

[10] J.L. Zeng, Z. Cao, D.W. Yang, L.X. Sun, L. Zhang, Thermal conductivity enhancement of Ag nanowires on an organic phase change material, J. Therm. Anal. Calorim. 101 (2010) 385–389, https://doi.org/10.1007/S10973-009-0472-Y.

[11] K.W. Shah, A review on enhancement of phase change materials - a nanomaterials perspective, Energy Build. 175 (2018) 57–68, https://doi.org/10.1016/J.ENBUILD.2018.06.043.

[12] P. Song, D. Wen, Experimental the oxidation of tin nanoparticles, J. Phys. Chem. C 113 (2009) 13470–13476, https://doi.org/10.1021/jp902580s.

[13] B. Thiel, R. Helbig, Growth of SnO2 single crystals by a vapour phase reaction method, J. Cryst. Growth 32 (1976) 259–264, https://doi.org/10.1016/0022-0248(76)90040-3.

[14] H. Mahmood, M.A. Khan, B. Mohuddin, T. Iqbal, Solution-phase growth of tin oxide (SnO2) nanostructures: structural, optical and photocatalytic properties, Mater. Sci. Eng., B 258 (2020), 114568, https://doi.org/10.1016/J.MSEB.2020.114568.

[15] A. Sharma, A. Khosla, S. Arya, Synthesis of SnO2 nanowires as a reusable and flexible electrode for electrochemical detection of riboflavin, Microchem. J. 156 (2020), 104858, https://doi.org/10.1016/J.MICROC.2020.104858.

[16] Q. Xie, Y. Zhu, P. Zhao, Y. Zhang, S. Wu, One-pot hydrothermal fabrication and enhanced lithium storage capability of SnO2 nanorods intertangled with carbon nanotubes and graphene nanosheets, J. Mater. Sci. 53 (2018) 1–11, https://doi.org/10.1007/S10853-018-2224-5/TABLES/1.

[17] T.M. Al-Saadi, B.H. Hussein, A.B. Hasan, A.A. Shehab, Study the structural and optical properties of Cr doped SnO2 nanoparticles synthesized by sol-gel method, Energy Proc. 157 (2019) 457–465, https://doi.org/10.1016/J.EGYPRO.2018.11.210.

[18] A.K. Vivekanandan, K. Azher, S.F. Chang, S.H. Chen, Size-controllable zinc oxide nanowires fabricated via the combination of die-casting and oxidation process, J. Alloys Compd. 861 (2021), 157964, https://doi.org/10.1016/j.jallcom.2020.157964.

[19] K.A. Borup, J. De Boor, H. Wang, F. Drymiotis, F. Gascoin, X. Shi, L. Chen, M.I. Fedorov, E. Müller, B.B. Iversen, G.J. Snyder, Measuring thermoelectric transport properties of materials, Energy Environ. Sci. 8 (2015) 423–435, https://doi.org/10.1039/C4EE01320D.

[20] S.H. Chen, C.C. Chen, C.G. Chao, Novel morphology and solidification behavior of eutectic bismuth-tin (Bi-Sn) nanowires, J. Alloys Compd. 481 (2009) 270–273, https://doi.org/10.1016/j.jallcom.2009.03.107.

[21] J.S. Kim, M.Y. Huh, J.P. Ahn, Effect of Particle Size on the Oxidation Behavior of Nanophase Tin Synthesized by Inert Gas Condensation, (n.d.). https://doi.org/10.4028/www.scientific.net/SSP.119.9.

[22] Z.Q. Jin, Y. Ding, Z.L. Wang, Mechanical behavior and magnetic separation of quasi-one-dimensional Sn O2 nanostructures: a technique for achieving monosize nanobelts/nanowires, J. Appl. Phys. 97 (2005), https://doi.org/10.1063/1.1882774.

[23] X.L. Ma, Y. Li, Y.L. Zhu, Growth mode of the SnO2 nanobelts synthesized by rapid oxidation, Chem. Phys. Lett. 376 (2003) 794–798, https://doi.org/10.1016/S0009-2614(03)01081-9.

[24] N. Gao, J. Cao, C. Wang, Z. Gao, R. Li, G. Ding, H. Ma, Y. Wang, L. Zhang, Study on the crystallinity and oxidation states of nanoporous anodized tin oxide films regulated by annealing treatment for supercapacitor application, Langmuir 38 (2021) 164–173, https://doi.org/10.1021/ACS.LANGMUIR.1C02304.

[25] G.S. Harlow, J. Drnec, T. Wiegmann, W. Lipé, J. Evertsson, A.R. Persson, R. Wallenberg, E. Lundgren, N.A. Vinogradov, Observing growth under confinement: Sn nanopillars in porous alumina templates, Nanoscale Adv. 1 (2019) 4764–4771, https://doi.org/10.1039/C9NA00473.

[26] L. Kong, J. Ma, Z. Zhu, C. Luan, X. Yu, Q. Yu, Synthesis of orthorhombic structure epitaxial tin oxide film, Mater. Lett. 64 (12) (2010) 1350–1353, https://doi.org/10.1016/j.matlet.2010.03.058.

[27] Y. Rangraz, S.M. Vahdat, S. Khaksar, SnO2 nanoparticles: a recyclable and heterogeneous catalyst for Pechmann condensation of coumarins and Knoevenagel condensation–Michael addition of biscoumarins, Heliyon 9 (2023), e15135, https://doi.org/10.1016/j.heliyon.2023.e15135.

[28] Y.X. Chen, L.J. Campbell, W.L. Zhou, Self-catalytic branch growth of SnO2 nanowire junctions, J. Cryst. Growth 270 (2004) 505–510, https://doi.org/10.1016/j.jcrysgro.2004.07.011.

[29] A.K. Vivekanandan, C.W. Lee, R.Z. Wu, W.H. Tsai, S.H. Chen, Y.Y. Chen, C.T. Lin, Tailoring InSb nanowires for high thermoelectric performance using AAO template-assisted die casting process, Nanomaterials 12 (2022), https://doi.org/10.3390/NANO12122032/S1, 2032.

[30] L. Alinauskas, E. Brooke, A. Regoutz, A. Katelnikovas, R. Raudonis, S. Yitzchaik, D.J. Payne, E. Garskaite, Nanostructuring of SnO₂ via solution-based and hard template assisted method, Thin Solid Films 626 (2017) 38–45, https://doi.org/10.1016/J.TSF.2017.02.015.

[31] W. Matysiak, T. Tański, W. Smok, O. Polishchuk, Synthesis of hybrid amorphous/crystalline SnO2 1D nanostructures: investigation of morphology, structure and optical properties, 2020, Sci. Rep. 10 (2020) 1–10, https://doi.org/10.1038/s41598-020-71383-2, 1–10.

[32] R.S. Sabry, R. Alobaidi, Template assisted synthesis of SnO2 nanorods by immerse and filtration technique, vacuum and drop setting, J. Mater. Sci. Mater. Electron. 27 (2016) 10036–10044, https://doi.org/10.1007/S10854-016-5075-3/METRICS.

[33] A. Sadeghzadeh-Attar, M.R. Bafandeh, The effect of annealing temperature on the structure and optical properties of well-aligned 1D SnO2 nanowires synthesized using template-assisted deposition, CrystEngComm 20 (2018) 460–469, https://doi.org/10.1039/C7CE01815K.

[34] V. Kumar, S. Sen, K.P. Muthe, N.K. Gaur, S.K. Gupta, J.V. Yakhmi, Copper doped SnO2 nanowires as highly sensitive H2S gas sensor, Sens. Actuators, B 138 (2009) 587–590, https://doi.org/10.1016/J.SNB.2009.02.053.

[35] G.G. Khan, S. Ghosh, K. Mandal, Origin of room temperature d0 ferromagnetism and characteristic photoluminescence in pristine SnO2 nanowires: a correlation, J. Solid State Chem. 186 (2012) 278–282, https://doi.org/10.1016/J.JSSC.2011.11.038.

[36] P. Chetri, A. Choudhury, Investigation of optical properties of SnO2 nanoparticles, Physica E Low Dimens Syst Nanostruct 47 (2013) 257–263, https://doi.org/10.1016/J.PHYSE.2012.11.011.